

# A Soft Resistive Acoustic Sensor Based on Suspended Standing Nanowire Membranes with Point Crack Design

Shu Gong, Lim Wei Yap, Yi Zhu, Bowen Zhu, Yan Wang, Yunzhi Ling, Yunmeng Zhao, Tiance An, Yuerui Lu, and Wenlong Cheng\*

An artificial basilar membrane (ABM) is an acoustic transducer that mimics the mechanical frequency selectivity of the real basilar membrane, which has the potential to revolutionize current cochlear implant technology. While such ABMs can be potentially realized using piezoelectric, triboelectric, and capacitive transduction methods, it remains notoriously difficult to achieve resistive ABM due to the poor frequency discrimination of resistive-type materials. Here, a point crack technology on noncracking vertically aligned gold nanowire (V-AuNW) films is reported, which allows for designing soft acoustic sensors with electric signals in good agreement with vibrometer output—a capability not achieved with corresponding bulk cracking system. The strategy can lead to soft microphones for music recognition comparable to the conventional microphone. Moreover, a soft resistive ABM is demonstrated by integrating eight nanowire-based sensor strips on a soft trapezoid frame. The wearable ABM exhibits high-frequency selectivity in the range of 319–1951 Hz and high sensitivity of 0.48–4.26 Pa<sup>-1</sup>. The simple yet efficient fabrication in conjunction with programmable crack design indicates the promise of the methodology for a wide range of applications in future wearable voice recognition devices, cochlea implants, and human–machine interfaces.

array inserted in the cochlea.<sup>[2]</sup> The conventional CI can sometimes cause complications including discomfort caused by the use of extracorporeal devices, nerve injury and tinnitus due to their mechanical mismatch between rigid CI electrode and soft tissue.

Soft acoustic sensors have potential to be used as soft microphones to replace the microphone in the extracorporeal devices of conventional CI to enable comfort wearable experience. In addition, soft artificial basilar membrane (ABM) has also been developed in recent years to potentially overcome the limitations of conventional CIs.<sup>[3–8]</sup> ABMs are acoustic sensors integrated on an artificial membrane that mimic the passive frequency selectivity and acoustic-to-electric energy conversion of hair cells in the organ of Corti. Soft ABM can be potentially implanted in the human cochlea to directly stimulate the auditory nerves, which is much softer, lighter than the conventional rigid CI electrodes.

Consequently, it may prevent nerve injury and tinnitus caused by modulus mismatch between inner ear tissues and conventional CI electrodes. Based on the understanding of frequency-specific wave travelling in human cochlea system,<sup>[9]</sup> an ABM can be designed to mimic cochlear tonotopy by adjusting structural parameters of active materials including piezoelectric,<sup>[3,6–8]</sup> triboelectric,<sup>[5]</sup> and capacitive<sup>[10]</sup> materials. These structural parameters include width, thickness, and stiffness in membranes,<sup>[3]</sup> beams,<sup>[5,8]</sup> and cantilevers.<sup>[4,7]</sup>

Unlike the aforementioned active materials, resistive-based materials are not yet used for designing soft ABM. Compared to capacitive, piezoelectric, and triboelectric-based devices, the advantage of the resistive devices lies at low cost in fabrication, facile device integration and single layered structure, which enables simplified design for the construction of ultrathin and ultrasoft tattoo-like devices without introducing additional material interfaces.<sup>[11,12]</sup> However, resistive-materials-based ABM have not been realized because of their poor frequency discrimination despite of intensive recent attempts.<sup>[13–16]</sup> Nanomaterials have provided new possibilities for the design and fabrication of wearable and stretchable electronic devices.<sup>[17–19]</sup> A number of resistive nanomaterials including carbon nanotubes,<sup>[20,21]</sup> nanowires,<sup>[22]</sup> nanoparticles,<sup>[23]</sup> nanosheet,<sup>[24]</sup> and graphene<sup>[25]</sup> have been used for sensing acoustic vibrational forces, indicating


## 1. Introduction

About 10% of the global population suffered from moderate or severe hearing impairment.<sup>[1]</sup> The current treatment is via a cochlear implant (CI), which can convert acoustic energy into electricity to stimulate auditory nerves through an electrode

Dr. S. Gong, Dr. L. W. Yap, Dr. B. Zhu, Dr. Y. Wang, Dr. Y. Ling,  
Dr. Y. Zhao, T. An, Prof. W. Cheng  
Department of Chemical Engineering  
Monash University  
Clayton, Victoria 3800, Australia  
E-mail: wenlong.cheng@monash.edu

Dr. S. Gong, Dr. L. W. Yap, Dr. B. Zhu, Dr. Y. Wang, Dr. Y. Ling,  
Dr. Y. Zhao, T. An, Prof. W. Cheng  
The Melbourne Centre for Nanofabrication  
Clayton, Victoria 3800, Australia

Y. Zhu, Prof. Y. Lu  
Research School of Engineering  
College of Engineering and Computer Science  
Australian National University  
Canberra, ACT 0200, Australia

 The ORCID identification number(s) for the author(s) of this article can be found under <https://doi.org/10.1002/adfm.201910717>.

DOI: 10.1002/adfm.201910717

the potential for voice recognition applications.<sup>[26]</sup> Crack-based design holds great promise for resistive materials to detect the frequency changes of acoustic signals due to their ultrahigh sensitivity in the ultralow vibrational strain range.<sup>[27,28]</sup> However, these noncracked or bulk-level cracked resistive films have not yet demonstrated the capability of correlating electrical signals with sound-induced membrane vibration at specific location. A possible reason is that local deformation may not be uniform or synchronized under acoustic vibrational forces.

Here, we demonstrate that a suspended point-cracked V-AuNWs membrane could be used to detect out-of-plane acoustic vibration forces with excellent acoustic frequency discrimination. The soft acoustic sensor was capable of distinguishing sound with both static and dynamic frequencies up to 3000 Hz. Our suspended local cracked V-AuNWs membrane could achieve sensitive yet specific resistive response to acoustic vibrations in excellent agreement with vibrometer output, which is not possible to achieve with corresponding bulk-cracking and noncracking design. This allows for designing a nanowire-based microphone with comparable performance to conventional microphone in an ultrathin and ultrasoft manner. In addition, the acoustic sensor could recover its conductance after releasing from an extensive strain of 50%, which opens a new route to design tattoo-like skin-conformal microphone. Furthermore, we demonstrate the first proof-of-concept soft resistive ABM with high-frequency selectivity in the range of 319–1951 Hz, and extremely high sensitivity of 0.48–4.26 Pa<sup>-1</sup>. Our point-cracking design in standing nanowires offers higher electrical outputs than previous piezoelectric or triboelectric-type ABM, which can be easily detected without the need of additional signal amplification. The comparison of our proposed device and the state-of-the-art acoustic sensors is shown in Table S1 (Supporting Information). While it is exciting to see the encouraging process in developing soft acoustic sensors, it is highly challenging to achieve simultaneously low device thickness, high stretchability, high sensitivity, high-frequency resolution, and frequency selectivity in a single system. However, such features are critical for the next-generation ultrathin, ultrasoft, and stretchable acoustic sensors and ABM for skin-conformal wearable devices.

## 2. Results and Discussion

We have recently demonstrated vertically aligned enokitake-like gold nanowires (V-AuNWs) bonded elastomeric sheets which exhibit much higher stretchability than corresponding lying-down nanowires or bulk metallic films.<sup>[29,30]</sup> This is because of their accordion fan-like structure upon deformation, which could effectively prevent catastrophic cracking unlike the continuous metallic film such as platinum<sup>[27,28]</sup> and gold.<sup>[31]</sup> V-AuNWs grown on the poly(methyl methacrylate) (PMMA) modified silicon wafer can be embedded in ultrathin polydimethylsiloxane (PDMS), obtaining highly conductive and strain-insensitive gold conductors (Figure S1, Supporting Information).<sup>[32]</sup> The V-AuNWs embedded PDMS membrane is confirmed by cross-sectional scanning electron microscope (SEM) image (Figure S2, Supporting Information).

Next, the ultrathin V-AuNWs membrane is transferred onto an Eco-flex elastomer with the assistance of a water dissolvable

polyvinyl alcohol (PVA) tape. We can introduce localized channel crack in the center of the V-AuNWs strip by sputtering a layer of silver onto the specific location through shadow masks followed by repeated tensile stretching (Figure 1a). The location without silver coating will not generate any cracks (Figure S3, Supporting Information). Silver layer could be dissolved by hydrogen peroxide/ammonium hydroxide solution, leaving localized parallel channel crack replicas (Figure 1b and Figure S3, Supporting Information). The soft nanowire-based acoustic sensor was obtained by transferring the ultrathin membrane onto a hole patterned PDMS frame.

As shown in Figure 1c, the V-AuNWs conductive strip showed dramatic resistance increase to the tensile strain because of the known crack enlargement (Figure S4, Supporting Information). The cracked area lost its conductivity completely after a tensile strain of more than 10%. However, its electrical conductance could be fully recovered after releasing from an extensive strain of 50% (Figure 1c). The excellent reproducibility of the point cracks technology was demonstrated by fabricating eight samples under the same conditions (100 nm silver layer, 30% repeated tensile stretching for 10 cycles). The sensitivity and stretchability of all eight sensors showed negligible deviation during the test (Figure S5, Supporting Information). The load-unload curves of the V-AuNWs/PDMS films with point cracks as a function of the applied strain of 20% is shown in Figure S6 (Supporting Information), demonstrating negligible hysteresis. In addition, the sensor exhibited stable resistive changes under both small (1% strain for 5000 cycles) and large (50% strain for 1000 cycles) repeated strain (Figure S7, Supporting Information). This high durability under high repeated strain test is in contrast with previous reported sputter coated metallic channel crack system, which could only allow a limited stretchability of < 10%.<sup>[27,28,31,33]</sup>

When a uniaxial strain is applied, the sensor becomes compressed transversally. Consequently, the longitudinal extension strain widens the gaps while the transverse compression force causes the cracks to dislocate. The simplified crack gaps evaluation under mechanical strain is illustrated in Figure S8 (Supporting Information). Without a strain, no cracking gaps are expected for our gold nanowire films. When a small strain is applied, the cracking gap at longitudinal direction is generated while the slightly dislocated cracking edges are still connected. When a large strain is applied, the dislocated cracking edges become disconnected, leading to more obvious increase in the resistance. The three scenarios may well explain the three gauge factor values of our acoustic sensors (Figure S6, Supporting Information).

For a specific crack on the elastomeric thin film, the crack width  $\sigma$  can be written as<sup>[27]</sup>

$$\sigma = \left( \frac{4\varepsilon d}{E'} \right) V(\delta) \quad (1)$$

where  $\varepsilon$  is the applied stress,  $d$  is the crack depth,  $\delta$  is the relative crack depth ( $\delta = d/t$ ) defined as the ratio of crack depth ( $d$ ) to sensor thickness ( $t$ ).  $E'$  is the effective modulus of the substrate. Here  $V(\delta)$  is the structural deformation of the crack interface in elastic deformation range, which could be estimated by Equation S1 (Supporting Information). For a particular sensor, this equation predicts that the crack width is proportional to

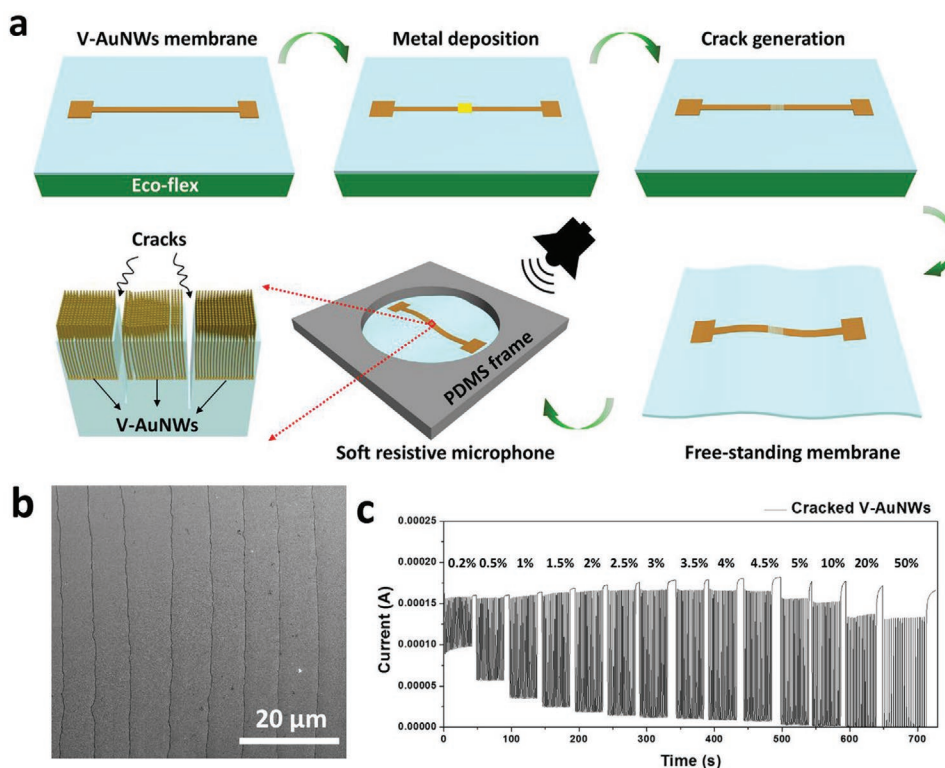


**Figure 1.** Fabrication process and characterization of V-AuNWs/PDMS thin film with point cracks. a) Schematic of fabrication process of point cracks in the middle of V-AuNWs thin film. b) Scanning electron microscopy image of the cracked area. c) The current changes of the middle-cracked thin film with dynamic tensile strain from 0.2–50%. 10 cycles of stretching-releasing test are conducted for each strain.

the applied strain, which is in good agreement with the experimental data (Figure S9, Supporting Information). We also used finite-element method (FEM) to model (Abaqus software; CAE 6.13-1) the crack opening with a crack height of 500 nm in a 10 μm thickness PDMS thin film (Figure S9a, Supporting Information). The FEM results showed high consistency with our SEM results (Figure S9b, Supporting Information). In addition, the relationship between the conductance and applied strain of the cracked thin film was calculated, which fits well with the experimental data (red line in Figure S9b, Supporting Information).

Previously reported cracked E-skin can offer sufficiently high sensitivity to identify subtle mechanical signals such as acoustic vibrations.<sup>[28]</sup> However, the bulk cracking system can hardly monitor acoustic vibration of a specific spot due to the challenges in crack control. By virtue of localized cracked technology, the electrical output of our middle-cracked gold E-skin showed high correlation to the mechanical vibration of a specific spot using a scanning laser Doppler vibrometer (LDV).<sup>[34]</sup> As shown in **Figure 2**, for the input sound pressure with a periodic chirp signal in a frequency range of 40–3000 Hz, the noncracked membrane is not sensitive enough to sense the acoustic signal (Figure 2a,d), while the fully cracked membrane showed poor correlation with the raw acoustic signals (Figure 2b,e), possibly because the acoustic strain level is neither evenly distributed along the membrane strip nor synchronized. In contrast, the local-cracked membrane exhibited resistive responses in excellent agreement with the raw

signals from the laser Doppler vibrometer (Figure 2c,f). The vibrometer output in Figure 2d–f are fast Fourier transform (FFT) signals where the signal is essentially modulated getting rid of the negative values. Fine details of Figure 2f were enlarged to show the sensor response toward the chirp signal at different frequencies. It was shown from the corresponding zoom-in curves (Figure 2g) that the detected frequencies were equal to the frequencies of the sound waves made by the sound source. In comparison, the noncracked sensor could only resolve a low-frequency sound ( $\approx 530$  Hz) while the fully cracked sensor could resolve a medium frequency sound ( $\approx 970$  Hz) but unable to resolve high-frequency sound at 2250 Hz (Figures S10 and 11, Supporting Information). It is worth noting that the resistance changes can hardly completely recover from one vibration before the start of the next vibration due to the hysteresis of the elastomeric materials. As a result, the sensor output is not like the sound displacement signal that changes all the way from positive to negative during a single vibration.

We further investigated the location-specific sensing signals from three different domains along the membrane for both fully cracked and middle-cracked samples. As shown in Figures S12 and S13 (Supporting Information), the sensor output of fully cracked sample exhibited poor correlation with the vibrational signals for all the three selected locations A, B and C. This could be because level of strain differed from center to end of the sensing strip, which caused spatial interference of resistive responses for the “all-sensitive” fully cracked sample. Such

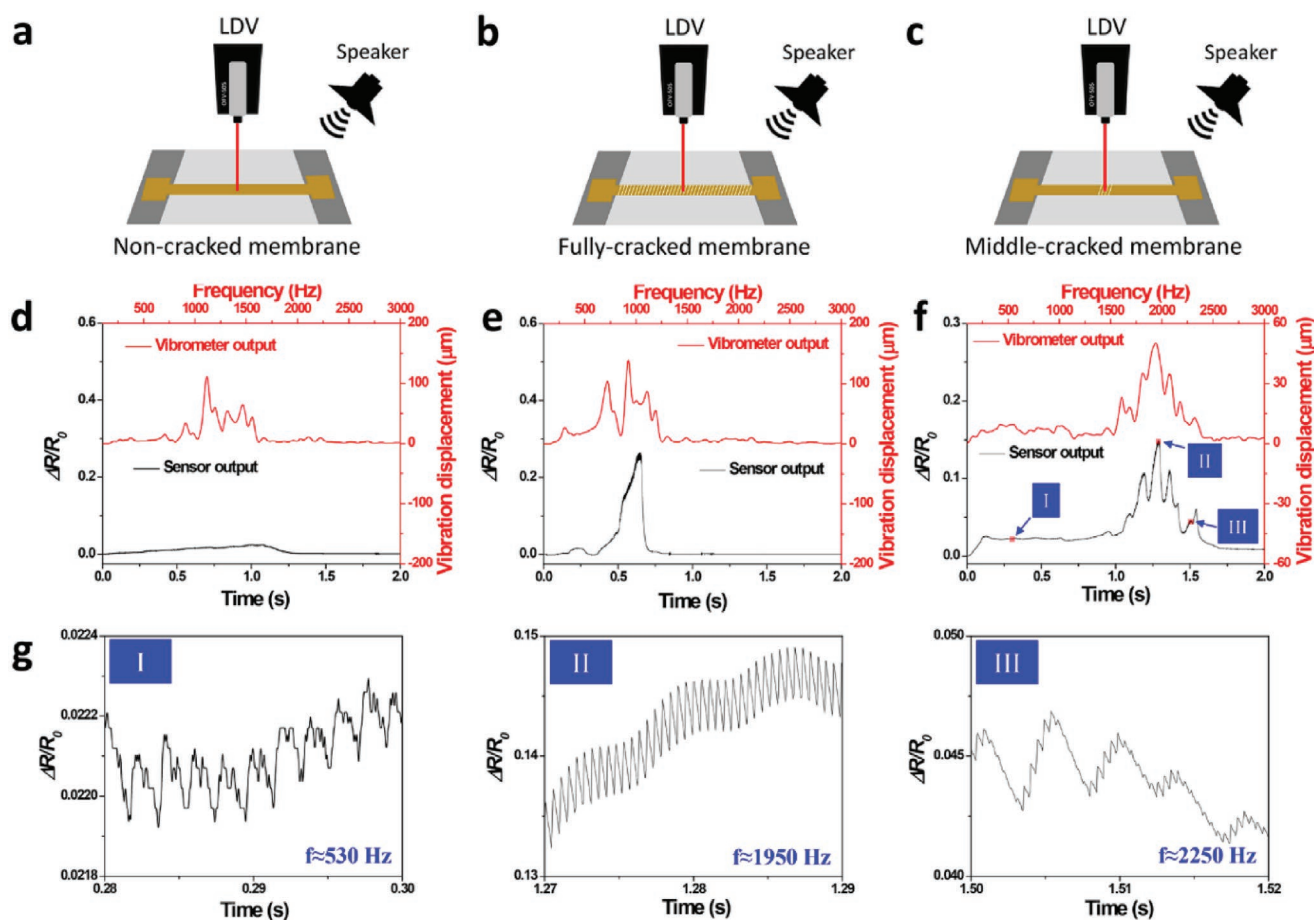


**Figure 2.** Sensing performance of various nanowire-based acoustic sensors. Schematic illustration of the experiment set-ups for acoustic measurement from a) sensor without cracks, b) sensor with uniform cracks, and c) sensor with localized cracks. Comparison of vibrometer output and sensor output from d) sensor without cracks, e) sensor with uniform cracks, and f) sensor with localized cracks under a chirp signal (40–3000 Hz) in 2 s. g) The enlarged view of resistance changes with time in three different time zones indicated in (f).

spatially averaged signals showed poor correlation with vibrational forces. In contrast, the specific “middle-sensitive” partially cracked sample only specifically identified the maximum straining point in the middle, therefore, led to high consistency with the vibrational signal with regards to both resonance frequency and signal intensity for the location B (Figure S13, Supporting Information). The resistance of noncracked locations A and C were insensitive to strains, therefore, showed poor correlation with the vibrational signals. The above results demonstrated significance of location-specific cracking for detecting specific acoustic vibrational signals.<sup>[11]</sup> Such high specificity is critically important for the construction of artificial basilar membrane.

We have previously reported that the size, depth, density and orientation of the cracked sensor can be well programmed using our local crack strategy.<sup>[11]</sup> Here we controlled the area and the density of the middle crack to evaluate the influence of the geometric factors of the thin film in response to an acoustic signal. As shown in Figure S14 (Supporting Information), the sensor with a crack area ratio of 1:10 and average crack spacing at 43  $\mu\text{m}$  showed the highest performance toward acoustic sound at 500 Hz in the SPL range of 70–95 dB.

We further monitored the electrical output from the nanowire-based acoustic sensor in response to sound coming from a speaker. The device exhibited stable and periodic electrical output across a frequency range between 50 and 1000 Hz, with the maximum resistance changes being obtained at 80 Hz, which is corresponding to the resonance frequency of the membrane. After that it exhibited a gradually decreasing trend with little fluctuation (Figure 3a). The typical dynamic resistance changes at a sound wave of frequency 400 Hz (intensity level 90 dB) is shown in Figure 3b. We used an FFT filtering technique to evaluate the noise signals from the background sound. As shown in Figure S15 (Supporting Information), the resistive output was very similar to the raw data after FFT filtering using the sound frequency. In contrast, the output was negligible when an FFT filtering beyond the sound frequency was used. The results suggested that the sensor output mainly came from the sound waves. Then we monitored the variations in the output resistance changes of the device with a decreasing sound pressure level (SPL) at frequencies of 500 and 1000 Hz to determine their minimum sound-detection capability (Figure 3c). We further evaluate the sensor performance in response to a tone with a large constant frequency range (Figure S16,

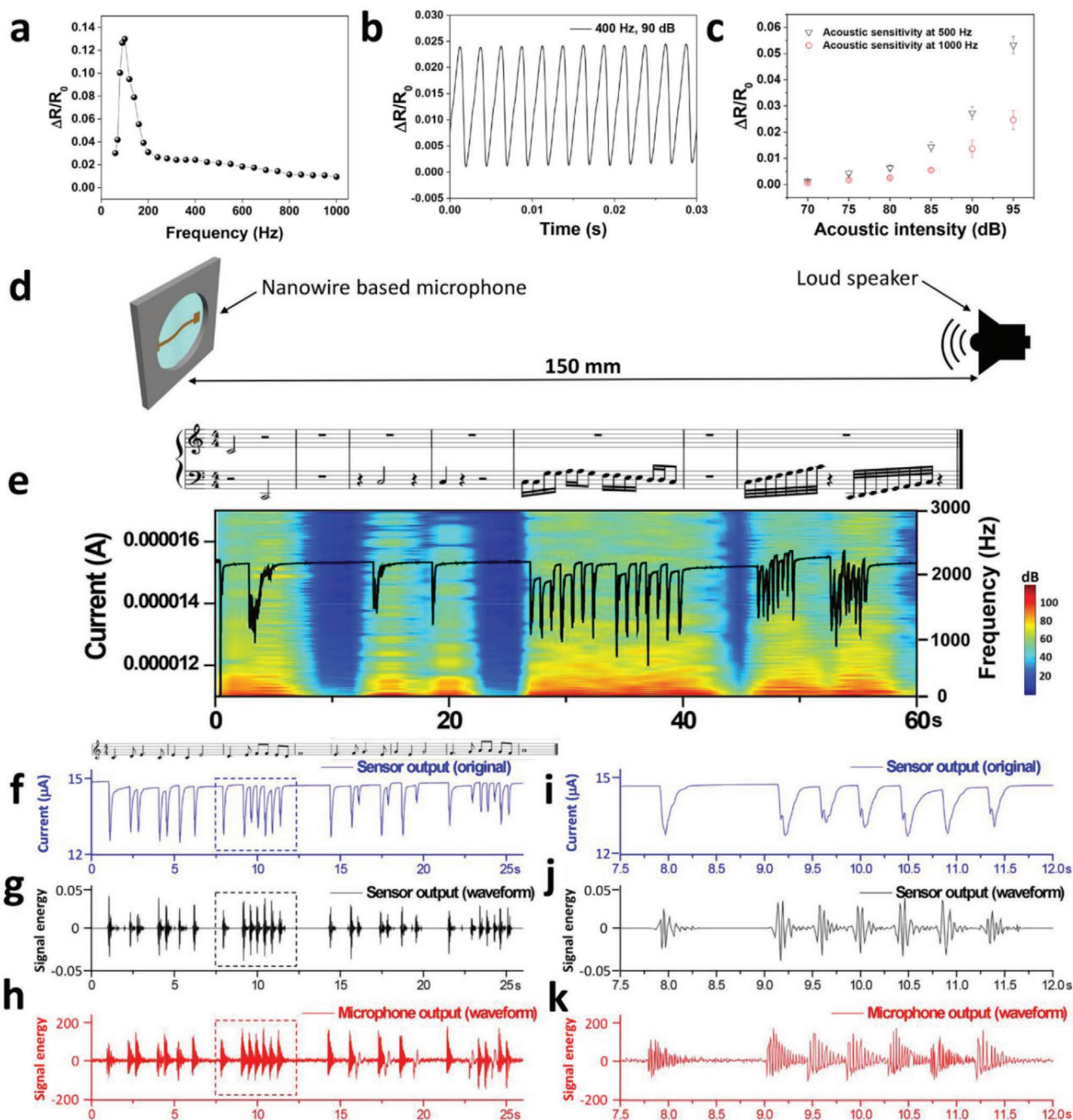


**Figure 3.** Characterization of point cracked nanowire-based acoustic sensor. a) Variation in resistance changes of the device with as a function of sound frequency from 0 to 1000 Hz. b) Resistance outputs of the device under sound with a constant frequency of 400 Hz at SPL of 90 dB. c) Variation in resistance changes of the device with a constant frequency of 80 Hz at SPL from 70 to 95 dB. d) Schematic of the experiment set-up of the music detection. e) The sensor output (curve) and the STFT analysis (background) in response to notes with different musical scale. f) The sensor output, g) waveform, and h) conventional microphone waveform in response to a piece of music. i–k) Enlarged curves from the same section in (f)–(h).

Supporting Information). Fine details of the sound frequency can be well demonstrated by the repeated pulse waveform up to 3000 Hz (Figure S16c, Supporting Information). The response of our sensor is quite uniform in the frequency range of 200–2000 Hz, which is the most commonly used frequency range to detect human speech. It is worth noting that the sensitivity

of our cracked acoustic sensor is also highly dependent on the thickness of freestanding membrane (Figure S17, Supporting Information). In this study, we use a PDMS with a typical thickness of 10  $\mu\text{m}$  to achieve high sensing performance.

By suspending an ultrathin free-standing cracked gold E-skin patches over a 3D printed frame (Figure 3d), we could

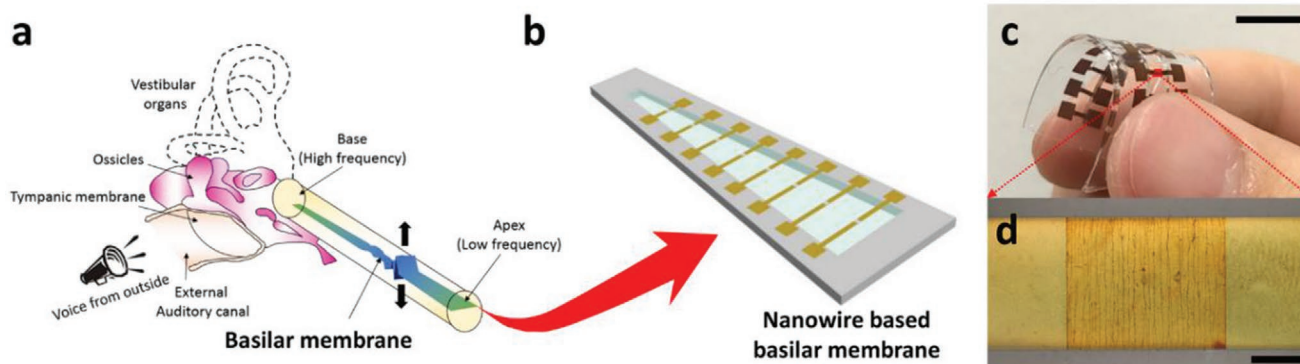


**Figure 4.** Design of nanowire-based soft ABM. a) Conceptual schematic of human ear with an uncoiled cochlea. b) Schematic of our nanowire-based artificial basilar membrane composed of eight sensor strips with localized cracks in the center. c) Photograph of the soft nanowire-based artificial basilar membrane. Scale bar: 1 cm. d) Optical image of the cracked area. Scale bar: 200  $\mu\text{m}$ .

identify various music notes 150 mm away from a loudspeaker (Figure 3e and Movie S1, Supporting Information). The resistance changes of our sensor (curve in Figure 3e) agreed very well with the spectrograms of the music sound (background in Figure 3e). We further measured different notes from the loudspeaker and performed an FFT analysis to the sensor output (Figure S18, Supporting Information). The signal-to-noise level of the acoustic sensor in response to music notes is  $3.15 \pm 0.64$  after applying an FFT filter with bandwidth of 2 Hz within the range of detected frequency (Figure S19, Supporting Information). The sensor output in response to musical notes at a constant SPL (80 dB) is repeatable after more than 1000 cycles (Figure S20, Supporting Information), indicating good durability toward acoustic vibration of our crack-based sensors. Moreover, a piece of music with continuous notes is measured by our nanowire-based acoustic sensor and a commercial microphone simultaneously (Figure 3f–k). The time-dependent waveform of the output current was obtained through the wavelet transform function in MATLAB (Figure 3f,g), which are in agreement with that of the commercial microphone. We further compared the short-time Fourier transform (STFT) signals of two devices. The nanowire-based device exhibited distinguishable frequencies for each note in a piece of music, while there were some discrepancies in the spectrogram of the commercial microphone (Figure S21, Supporting Information). Moreover, the as-measured wave shape by our sensors was very close to the wave shape of the original sound (Figure S22, Supporting Information), indicating the potential of recovery the raw sound.

The passive frequency selectivity of a basilar membrane in human cochlea is achieved through varying its width, thickness, and stiffness along the length of the cochlear. High-frequency sounds will be amplified near the base of the cochlea, while low-frequency sounds will be amplified near the apex (Figure 4a).<sup>[9]</sup> The outstanding performance of our middle-point-cracked V-AuNW membrane motivated us to design a resistive artificial basilar membrane, by varying the length of sensors along a trapezoid frame (Figure 4b). Detailed fabrication procedure can be found in Figure S23 (Supporting Information). We could obtain a prototype device that is soft and durable owing to the V-AuNW-embedded design (Figure 4c,d).

Acoustic responses of each sensor strip in the resistive trapezoid ABM were recorded and analyzed (Figure 5a). A speaker was used to produce a chirp sound in the frequency range of 40–3000 Hz for a duration of 2 s with  $\approx 82$ –88 dB of sound pressure. The typical resistance change of a sensor strip is shown in Figure 5b, where the signal could be converted to waveform (Figure 5c) and STFT signal (Figure 5d) with the highest peak at 575 Hz, reflecting the resonance frequency of the first harmonic mode in the middle of this beam. The harmonic series (2nd, 3rd, 4th, 5th ... harmonic modes) of fundamental frequency could also be detected by our sensor (Figure 5d), in which the frequency of each sound is an integer multiple of the first harmonic frequency. As harmonic mode increases, the vibration amplitude is likely to be weakened subsequently.<sup>[35]</sup> This phenomenon is consistent with the weakened intensity of our sensor signal (Figure 5d).

The measured mechanical displacement of the nanowire-based ABM was normalized by applied sound pressure. The acoustic-to-mechanical energy transfer function could be defined as  $H_{\text{PD}}$ <sup>[5]</sup>

$$H_{\text{PD}}(f) = \frac{D(f)}{P(f)} \quad (2)$$

where  $P$  is the sound pressure,  $D$  is the mechanical displacement at the geometric center of the sensor strip, and  $f$  is the frequency of sound. Waterfall plots of  $H_{\text{PD}}$  for all sensor strips are shown in Figure 5e. The peaks of the  $H_{\text{PD}}$  represent the resonance frequencies of the first bending mode for geometric center of each sensors (Figure 5e). Similar to human cochlea, the resonance frequencies of the transfer functions sequentially shift to lower frequencies with the increase of sensor strip length. It is worth noting that some distortion in the resonant peaks was observed. Such distortion became more severe for shorter sensor strips. The distortion is mainly attributed to the viscoelastic nature of the PDMS membrane and could be partially eliminated by transferring the ultrathin membrane to a relatively rigid polyimide (PI) membrane (Figure S24, Supporting Information). However, the use of additional PI layer will increase the stiffness and thickness of the overall device, leading to reduced resistance response toward acoustic

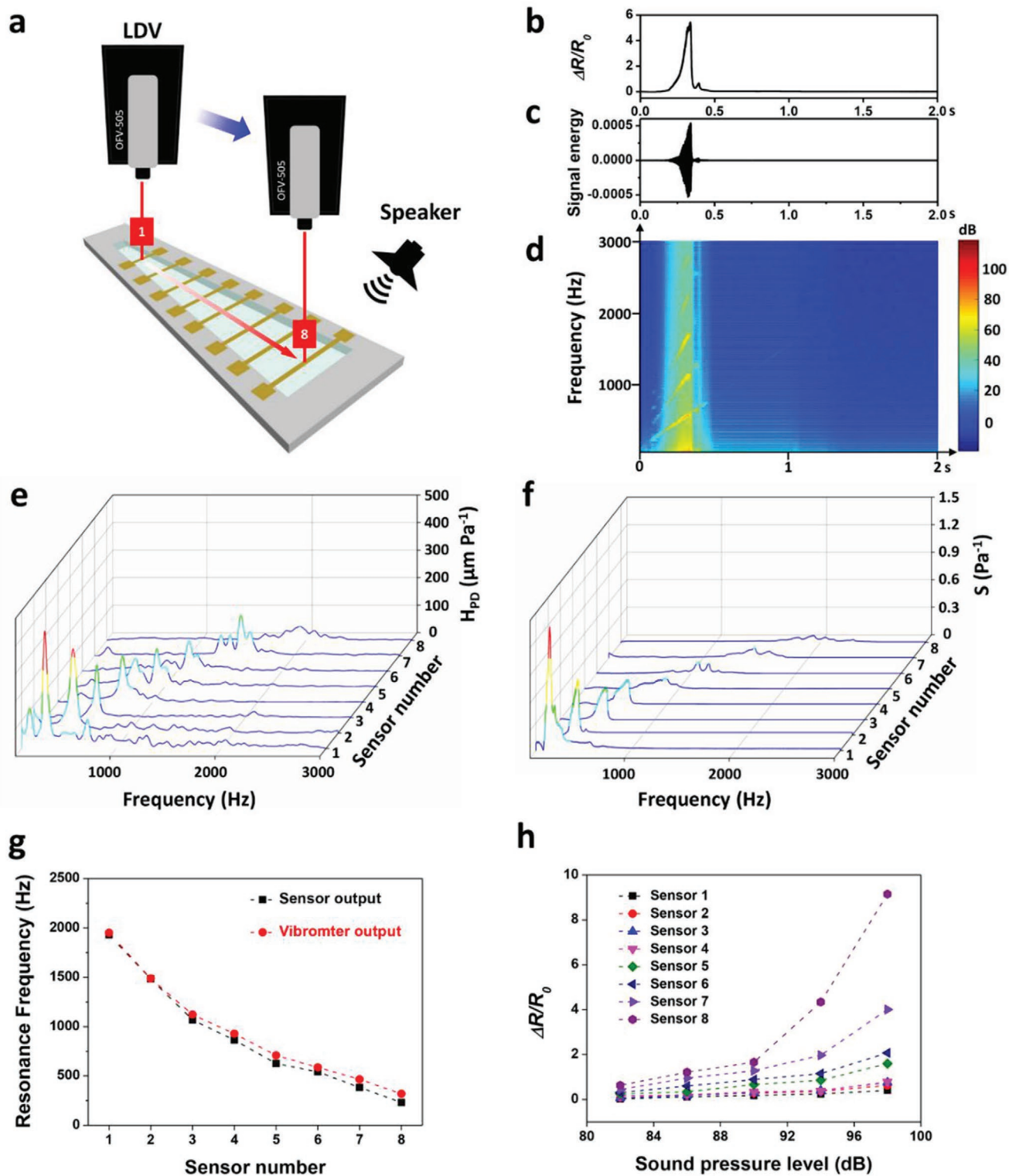


**Figure 5.** Characterization of Nanowire-based soft ABM. a) Schematic illustration of the experiment set-ups. b) Sensor resistance response, c) waveform, and d) STFT signals of sensor strip 7 under a chirp signal (40–3000 Hz) for 2 s. e) Acoustic-to-mechanical transfer function for all sensor strips in the frequency range from 40 to 3000 Hz. f) Sensitivity for all sensor strips in the frequency range from 40 to 3000 Hz. g) Resonance frequencies of the ABM determined from vibrometer output and sensor output. h) Dependence of the sensor output of our ABM on the sound pressure level when applying a pure tone at the resonance frequency of each sensor.

tones (Figure S25, Supporting Information). In addition, the sensitivity ( $S$ ) for acoustic sensors can be calculated by Equation (3)<sup>[36,37]</sup>

$$S = \frac{\Delta R/R_0}{P} = \frac{(R - R_0)/R_0}{P_0 \times 10^{L_p/20}} \quad (3)$$

where  $R$  and  $R_0$  are resistances of sensor before and after acoustic vibration, respectively.  $P_0$  is the reference sound pressure of 0.00002 Pa and  $L_p$  is the sound pressure level in decibel. The measured sensitivity of each sensor strips is plotted in Figure 5f. The sensitivities of nanowire-based ABM at the resonance frequencies were in the range of 0.48–4.26 Pa<sup>-1</sup>, which is much higher than most of resistive wearable pressure sensors<sup>[13,14,33,38–40]</sup> (0.00026–0.606 Pa<sup>-1</sup> in the pressure range of 0–6 kPa). The resonance frequencies measured from sensor output matches well with that in transfer function ( $H_{PD}$ ) with maximum error less than 10% (Figure 5g). In addition, the frequency range of our nanowire-based ABM falls in the human communication frequency range (300–3500 Hz),<sup>[7]</sup> which can be directly used for speech recognition. We further proved that the resonance frequency measured by peak value of sensor resistance changes is independent with frequency range and time range of the input chirp sound (Figure S26, Supporting Information), demonstrating the resonance frequency detected by our ABM is valid.

To identify the dynamic range of electrical outputs of our device toward acoustic stimulus with different sound pressure levels, a pure tone was applied to each sensor at its resonance frequency (Figure 5h). Highly distinguished signal is detected in the sound pressure range of 82–98 dB SPL. We also evaluated the sensor output at SPL lower than 82 dB SPL, as the SPL of 82–98 dB may contain high dB of noise level, making it difficult to verify the performance of the ABM. The minimum detectable SPL for our sensors was around 72 dB SPL (Figure S27, Supporting Information), below which almost no resistance changes can be detected. The insensitivity of the sensor at the low dB of noise level (<70 dB SPL) is possibly due to the use of elastomeric membrane (PDMS), which requires larger sound pressure to drive efficient vibration than its high-moduli counterparts. The validity of the fabricated nanowire-based ABM is further verified with a piece of voice in constant frequencies of 300 and 1000 Hz, respectively. As shown in Figure S28 (Supporting Information), sensor 8 exhibited the highest intensity upon 300 Hz pure tone, while the highest response toward 1000 Hz pure tone shifted to sensor 3. These results are highly consistent with their resonance frequencies as shown in Figure 5e.

### 3. Conclusion

In summary, we report on a resistive nanowire-based acoustic sensor from point crack technology. The generation of point cracks leads to ultrahigh acoustic sensitivity at selected area, which is difficult to achieve with previous uniformly distributed crack-based strain sensors. We further demonstrate the applications of our soft nanowire acoustic sensors for musical notes detection, which showed comparable performance with the conventional microphone. Then we developed a soft resistive ABM based on an array of nanowire strip sensors. The as-prepared devices exhibited both

high-frequency selectivity (319–1951 Hz) and acoustic sensitivity (0.48–4.26 Pa<sup>-1</sup>) within the human communication frequency range, beyond which we may find a myriad of additional applications in future smart soft ear prosthetics, voice security, voice-based drones and robots' control, artificial intelligence, and so on.

### 4. Experimental Section

**Chemicals:** Gold (III) chloride trihydrate (HAuCl<sub>4</sub>·3H<sub>2</sub>O, 99.9%), triisopropylsilane (99%), 4-mercaptobenzoic acid (MBA, 90%), (3-aminopropyl)triethoxysilane (APTES), sodium citrate tribasic dihydrate (99.0%), L-ascorbic acid, polymethyl methacrylate, photoresist (AZ1512), hexane, and ethanol (analytical grade) were purchased from Sigma-Aldrich. All solutions were prepared using deionized water. All chemicals were used as received unless otherwise indicated. Conductive wires were purchased from Adafruit.

**Synthesis of Vertically Alignment Gold Nanowires:** A modified seed-mediated approach was used, as described in the literature.<sup>[29,30]</sup> First, 2 nm gold seed were synthesized. Briefly, 0.25 mL 25 × 10<sup>-3</sup> M HAuCl<sub>4</sub>·3H<sub>2</sub>O and 0.147 mL × 10<sup>-3</sup> M sodium citrate was added into conical flask with 20 mL H<sub>2</sub>O under vigorous stirring. After 1 min, 600 μL of ice-cold 0.1 M NaBH<sub>4</sub> solution was added. The solution was then stirred for 5 min and stored at 4 °C until needed. To grow V-AuNWs on substrates (e.g., PMMA coated silicon wafer), O<sub>2</sub> plasma was applied for 5 min to render the surfaces hydrophilic. Then the substrates were functionalized with an amino group by immersed in a 5 × 10<sup>-3</sup> M APTES solution for 1 h. The substrate was further immersed into 2 nm gold seed solution for 2 h to ensure the saturated adsorption, followed by rinsing with water two times to remove excess seed particles. Finally, Au seed-anchored substrates were immersed in a growth solution containing 980 × 10<sup>-6</sup> M MBA, 12 × 10<sup>-3</sup> M HAuCl<sub>4</sub>, 29 × 10<sup>-3</sup> M L-ascorbic acid, leading to the formation of V-AuNWs thin films.

**Fabrication of Nanowire-Based Acoustic Sensors with Localized Cracks:** A thin PMMA layer was spin-coated on bare silicon wafer at 3000 rpm for 45 s and baked at 180 °C for 2 min. After synthesis of V-AuNWs on the PMMA surface followed the procedure demonstrated above, photoresist (AZ1512) was spin-coated on top of nanowires at 3000 rpm for 45 s, and electrodes patterns were formed via conventional photolithography and etching process. PDMS (w/w base: curing agent = 10: 1) was diluted with n-Hexane (w/w PDMS: n-Hexane = 1:3) and spin-coated on the top of patterned photoresist at 1000 rpm for 1 min. After curing at 80 °C for 3 h, the ultrathin V-AuNWs/PDMS film was lifted-off by sonicating the wafer in acetone solution for 30 s, which was finally fished up by a water-dissolvable PVA supporting paper. The ultrathin V-AuNWs/PDMS film was further transferred onto an Eco-flex substrate, which was covered by a shadow mask, leaving the desired area exposed for silver sputtering. A layer of silver thin film was sputtered with speed of 0.3 nm s<sup>-1</sup>. Localized channel cracks could be formed on the film after applying a repeated strain of for 10 cycles using a uniaxial moving stage (THORLABS Model LTS150/M). Silver thin film was then dissolved by hydrogen peroxide/ammonium hydroxide (1:1) solution. After that, the ultrathin cracked V-AuNWs/PDMS film was suspended onto a hold patterned PDMS frame.

**Fabrication of Nanowire-Based Acoustic Sensors with Uniform Cracks:** The fabrication process of uniform cracks on V-AuNWs/PDMS was similar to localized crack, except that the entire film was covered by a layer of silver thin film.

**Fabrication of Nanowire-Based ABM:** The fabrication process of nanowire-based ABM was similar to the acoustic sensor except that the pattern of photoresist mask was different. In the current design, the lengths of sensor strips 1–8 were kept at 2–5.5 mm (0.5 mm interval for each sensor strip) with a constant width of 0.5 mm. In addition, a PDMS trapezoid patterned PDMS frame was used.

**Characterization:** The SEM images were characterized using FEI Helios Nanolab 600 FIB-SEM operating at a voltage of 5 kV. To test the electro-mechanical responses of V-AuNWs/PDMS strain sensors, the two ends of the samples were attached to motorized moving stages



(THORLABS Model LTS150/M). Uniform stretching cycles were applied by a computer-based user interface (Thorlabs APT user), while the current changes were measured by a VERSASTAT 3–500 electrochemical system (Princeton Applied Research). For the acoustic sensing, a high sampling rate of 10000 was set to measure the current changes of samples with a constant voltage of 0.1 V. For the experiment set-ups of acoustic sensing, a loudspeaker was located beside (directions of loudspeaker and ABM were kept at 45°) the sensor to produce sound. A Compact Digital Sound Level Meter (Jaycar, QM1589) was fixed near the soft acoustic sensors and ABM to measure the SPL around the device. An LDV system (OFV-2570, Polytec) was equipped perpendicular to the geometric center of sensor strip along the longitudinal direction, thus measuring the displacement of each point upon chirp sound. The chirp sound was produced by Labview at sampling rate of 10000. For the music notes sensing, a commercial microphone was located near the nanowire-based acoustic sensor, which captured the sound emitted by the loudspeaker. The waveform was obtained through the wavelet transform function in MATLAB to decompose the sensor output. The waveform generated was the integral values of sensor output. The STFT analysis was conducted by applying an STFT function in MATLAB to decompose the sensor output. The FFT analysis was conducted by applying an FFT function in origin to decompose the sensor output.

## Supporting Information

Supporting Information is available from the Wiley Online Library or from the author.

## Acknowledgements

This research was financially supported under Discovery Projects funding scheme (DP180101715), Linkage Projects scheme (LP160100521), and Jack Brockhoff foundation (JBF Grant number 4659–2019). This work was performed in part at the Melbourne Centre for Nanofabrication (MCN) in the Victorian Node of the Australian National Fabrication Facility (ANFF).

## Conflict of Interest

The authors declare no conflict of interest.

## Keywords

acoustic sensors, artificial basilar membranes, point crack design, soft microphones, standing gold nanowires

Received: December 26, 2019

Revised: March 24, 2020

Published online: April 30, 2020

- [1] N. Oishi, J. Schacht, *Expert Opin. Emerging Drugs* **2011**, *16*, 235.
- [2] P. C. Loizou, *IEEE Eng. Med. Biol. Mag.* **1999**, *18*, 32.
- [3] H. S. Lee, J. Chung, G. T. Hwang, C. K. Jeong, Y. Jung, J. H. Kwak, H. Kang, M. Byun, W. D. Kim, S. Hur, S.-H. Oh, K. J. Lee, *Adv. Funct. Mater.* **2014**, *24*, 6914.
- [4] J. Jang, J. Lee, S. Woo, D. J. Sly, L. J. Campbell, J.-H. Cho, S. J. O'Leary, M.-H. Park, S. Han, J.-W. Choi, J. H. Jang, H. Choi, *Sci. Rep.* **2015**, *5*, 12447.
- [5] J. Jang, J. Lee, J. H. Jang, H. Choi, *Adv. Healthcare Mater.* **2016**, *5*, 2481.
- [6] T. Inaoka, H. Shintaku, T. Nakagawa, S. Kawano, H. Ogita, T. Sakamoto, S. Hamanishi, H. Wada, J. Ito, *Proc. Natl. Acad. Sci. USA* **2011**, *108*, 18390.
- [7] J. Jang, J. H. Jang, H. Choi, *J. Micromech. Microeng.* **2017**, *27*, 075006.
- [8] S. Kim, W. J. Song, J. Jang, J. H. Jang, H. Choi, *J. Micromech. Microeng.* **2013**, *23*, 095018.
- [9] G. von Békésy, *Nature* **1970**, *225*, 1207.
- [10] R. D. White, L. Cheng, K. Grosh, presented at *Microfluidics, BioMEMS, and Medical Microsystems III*, San Jose, CA January, **2005**.
- [11] S. Gong, L. W. Yap, B. Zhu, Q. Zhai, Y. Liu, Q. Lyu, K. Wang, M. Yang, Y. Ling, D. T. Lai, F. Marzbanrad, W. Cheng, *Adv. Mater.* **2019**, *31*, 1903789.
- [12] S. Gong, L. W. Yap, B. Zhu, W. Cheng, *Adv. Mater.* **2020**, *32*, 192278.
- [13] L. Pan, A. Chortos, G. Yu, Y. Wang, S. Isaacson, R. Allen, Y. Shi, R. Dauskardt, Z. Bao, *Nat. Commun.* **2014**, *5*, 3002.
- [14] S. Gong, W. Schwalb, Y. Wang, Y. Chen, Y. Tang, J. Si, B. Shirinzadeh, W. Cheng, *Nat. Commun.* **2014**, *5*, 3132.
- [15] J. Park, M. Kim, Y. Lee, H. S. Lee, H. Ko, *Sci. Adv.* **2015**, *1*, e1500661.
- [16] B. Zhu, Z. Niu, H. Wang, W. R. Leow, H. Wang, Y. Li, L. Zheng, J. Wei, F. Huo, X. Chen, *Small* **2014**, *10*, 3625.
- [17] T. Wang, Y. Guo, P. Wan, X. Sun, H. Zhang, Z. Yu, X. Chen, *Nanoscale* **2017**, *9*, 869.
- [18] P. Wan, X. Wen, C. Sun, B. K. Chandran, H. Zhang, X. Sun, X. Chen, *Small* **2015**, *11*, 5409.
- [19] S. Gong, W. Cheng, *Adv. Electron. Mater.* **2017**, *3*, 1600314.
- [20] T. Yamada, Y. Hayamizu, Y. Yamamoto, Y. Yomogida, A. Izadi-Najafabadi, D. N. Futaba, K. Hata, *Nat. Nanotechnol.* **2011**, *6*, 296.
- [21] Z. Liu, D. Qi, P. Guo, Y. Liu, B. Zhu, H. Yang, Y. Liu, B. Li, C. Zhang, J. Yu, B. Liedberg, X. Chen, *Adv. Mater.* **2015**, *27*, 6230.
- [22] S. Kang, S. Cho, R. Shanker, H. Lee, J. Park, D.-S. Um, Y. Lee, H. Ko, *Sci. Adv.* **2018**, *4*, eaas8772.
- [23] S. Zhang, L. Cai, W. Li, J. Miao, T. Wang, J. Yeom, N. Sepúlveda, C. Wang, *Adv. Electron. Mater.* **2017**, *3*, 1700067.
- [24] G.-H. Lim, N.-E. Lee, B. Lim, *J. Mater. Chem. C* **2016**, *4*, 5642.
- [25] L.-Q. Tao, H. Tian, Y. Liu, Z.-Y. Ju, Y. Pang, Y.-Q. Chen, D.-Y. Wang, X.-G. Tian, J.-C. Yan, N.-Q. Deng, Y. Yang, T.-L. Ren, *Nat. Commun.* **2017**, *8*, 14579.
- [26] H. Ding, X. Shu, Y. Jin, T. Fan, H. Zhang, *Nanoscale* **2019**, *11*, 5839.
- [27] B. Park, J. Kim, D. Kang, C. Jeong, K. S. Kim, J. U. Kim, P. J. Yoo, T. i. Kim, *Adv. Mater.* **2016**, *28*, 8130.
- [28] D. Kang, P. V. Pikhitsa, Y. W. Choi, C. Lee, S. S. Shin, L. Piao, B. Park, K.-Y. Suh, T.-i. Kim, M. Choi, *Nature* **2014**, *516*, 222.
- [29] Y. Wang, S. Gong, D. Gómez, Y. Ling, L. W. Yap, G. P. Simon, W. Cheng, *ACS Nano* **2018**, *12*, 8717.
- [30] Y. Wang, S. Gong, S. J. Wang, X. Yang, Y. Ling, L. W. Yap, D. Dong, G. P. Simon, W. Cheng, *ACS Nano* **2018**, *12*, 9742.
- [31] T. Yang, X. Li, X. Jiang, S. Lin, J. Lao, J. Shi, Z. Zhen, Z. Li, H. Zhu, *Mater. Horiz.* **2016**, *3*, 248.
- [32] B. Zhu, S. Gong, F. Lin, Y. Wang, Y. Ling, T. An, W. Cheng, *Adv. Electron. Mater.* **2019**, *5*, 1800509.
- [33] Y. W. Choi, D. Kang, P. V. Pikhitsa, T. Lee, S. M. Kim, G. Lee, D. Tahk, M. Choi, *Sci. Rep.* **2017**, *7*, 40116.
- [34] M. A. Ruggero, N. C. Rich, *Hear. Res.* **1991**, *51*, 215.
- [35] Y. Jung, J.-H. Kwak, Y. Lee, W. Kim, S. Hur, *Sensors* **2014**, *14*, 117.
- [36] M. Toda, M. L. Thompson, *IEEE Sens. J.* **2006**, *6*, 1170.
- [37] C. Lang, J. Fang, H. Shao, X. Ding, T. Lin, *Nat. Commun.* **2016**, *7*, 11108.
- [38] H. B. Yao, J. Ge, C. F. Wang, X. Wang, W. Hu, Z. J. Zheng, Y. Ni, S. H. Yu, *Adv. Mater.* **2013**, *25*, 6692.
- [39] H. Tian, Y. Shu, X.-F. Wang, M. A. Mohammad, Z. Bie, Q.-Y. Xie, C. Li, W.-T. Mi, Y. Yang, T.-L. Ren, *Sci. Rep.* **2015**, *5*, 8603.
- [40] B. Su, S. Gong, Z. Ma, L. W. Yap, W. Cheng, *Small* **2015**, *11*, 1886.